

Western University

Scholarship@Western

---

Civil and Environmental Engineering  
Publications

Civil and Environmental Engineering  
Department

---

2-1-2023

## Retrieval of Peak Thunderstorm Wind Velocities Using WSR-88D Weather Radars

Ibrahim Ibrahim  
*Western University*

Gregory A. Kopp  
*Western University*

David M.L. Sills  
*Western University, David.Sills@uwo.ca*

Follow this and additional works at: <https://ir.lib.uwo.ca/civilpub>

---

### Citation of this paper:

Ibrahim, Ibrahim; Kopp, Gregory A.; and Sills, David M.L., "Retrieval of Peak Thunderstorm Wind Velocities Using WSR-88D Weather Radars" (2023). *Civil and Environmental Engineering Publications*. 217.  
<https://ir.lib.uwo.ca/civilpub/217>

# Retrieval of Peak Thunderstorm Wind Velocities Using WSR-88D Weather Radars

IBRAHIM IBRAHIM,<sup>a</sup> GREGORY A. KOPP,<sup>a</sup> AND DAVID M. L. SILLS<sup>a</sup>

<sup>a</sup> Northern Tornadoes Project, Faculty of Engineering, Western University, London, Ontario, Canada

(Manuscript received 30 March 2022, in final form 17 October 2022)

**ABSTRACT:** The current study develops a variant of the VAD method to retrieve thunderstorm peak event velocities using low-elevation WSR-88D radar scans. The main challenge pertains to the localized nature of thunderstorm winds, which complicates single-Doppler retrievals as it dictates the use of a limited spatial scale. Since VAD methods assume constant velocity in the fitted section, it is important that retrieved sections do not contain background flow. Accordingly, the current study proposes an image processing method to partition scans into regions, representing events and the background flows, that can be retrieved independently. The study compares the retrieved peak velocities to retrievals using another VAD method. The proposed technique is found to estimate peak event velocities that are closer to measured ASOS readings, making it more suitable for historical analysis. The study also compares the results of retrievals from over 2600 thunderstorm events from 19 radar–ASOS station combinations that are less than 10 km away from the radar. Comparisons of probability distributions of peak event velocities for ASOS readings and radar retrievals showed good agreement for stations within 4 km from the radar while more distant stations had a higher bias toward retrieved velocities compared to ASOS velocities. The mean absolute error for velocity magnitude increases with height ranging between 1.5 and 4.5 m s<sup>-1</sup>. A proposed correction based on the exponential trend of mean errors was shown to improve the probability distribution comparisons, especially for higher velocity magnitudes.

**KEYWORDS:** Databases; Measurements; Radars/Radar observations; Surface observations

## 1. Introduction

### a. Background

The estimation of wind speeds, especially those associated with high-intensity weather events, is important for atmospheric scientists and wind engineers alike. While meteorologists and atmospheric scientists rely on measured wind speeds to issue appropriate weather warnings and to calibrate weather prediction models, wind engineers are concerned with providing suitable wind loads for the design of safe and reliable structures. Measured peak wind velocities are used to perform extreme value analysis on records that have sufficient historical extent. Efforts to evaluate statistical properties of wind speeds date back to Thom (1968). More advanced efforts emphasized the importance of separating statistical properties of wind phenomena with distinct scales (Gomes and Vickery 1976; Riera and Nanni 1989; Mason 2015). In other words, statistics related to thunderstorms, which are localized in nature, should be separated from statistics related to extratropical and tropical cyclones. When separated, statistics indicate that peak thunderstorm velocities tend to govern the annual maximum wind speeds for a vast region of the United States, spanning the Southeast all the way to the Midwest (Lombardo and Zickar 2019).

While different methods have been implemented, including those of Duranona (2015), Lombardo et al. (2009), Vallis et al. (2019), and Zhang et al. (2018), a common aspect in all studies

is that they rely on point measurements from anemometers. Networks of anemometers, like Automated Surface Observing Systems (ASOS) (NWS 2021a) and Automated Weather Observing System (AWOS) (FAA 2021), include wind records that go back decades. Standardization procedures, including unifying height, ground roughness, and averaging time, are performed so that data across different sites form a homogeneous dataset (Masters et al. 2010). The spacing of observing sites in such networks is often orders of magnitude larger than thunderstorms. Therefore, while single-point measurements can sufficiently describe the synoptic-scale wind for a region or thunderstorm winds at a single point, they are insufficient to describe 1) the spatial correlation between wind speeds measured at neighboring points, which is of importance to numerical weather prediction modeling efforts, and 2) the loading for spatially distributed structures such as electrical transmission lines, long-span bridges, or large industrial complexes. Resolving small-scale spatial correlations cannot be achieved by anemometers in the case of thunderstorms unless a dense network of anemometers is used. This is impractical to achieve in practice from an observational nonresearch focused network considering these applications require resolution between hundreds of meters to a few kilometers.

In contrast to networks of anemometers, weather Doppler radars provide measurements that have high spatial resolution. The use of Doppler radar data to estimate wind velocities can result in a grid of points with a spatial resolution that depends on factors like the scanning pattern, its frequency, pulse repetition frequency, antenna size, etc. In the case where the estimated velocities can be verified to be equivalent to those provided by anemometers, the results can provide insights on thunderstorm wind flow conditions.

 Denotes content that is immediately available upon publication as open access.

Corresponding author: Ibrahim Ibrahim, iibrah6@uwo.ca

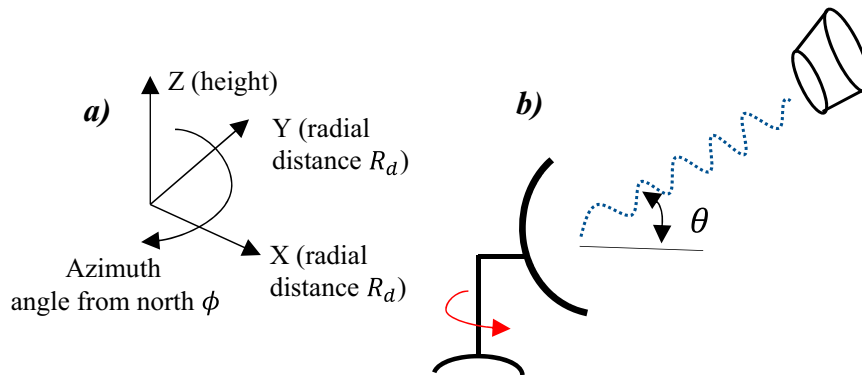


FIG. 1. (a) A schematic representation of coordinate system. (b) PPI scanning mode.

### b. Radar retrievals

Doppler weather radars measure velocity using the Doppler effect. The phase shift of the returning signal indicates the velocity toward or away from the radar depending on the phase sign. Weather radars operate in plan position indicator (PPI) scanning mode to capture horizontal plane scans. Figure 1 shows schematics of (Fig. 1a) the coordinate system used and (Fig. 1b) PPI scanning mode where radars scan around a vertical axis. Radar scan volumes combine several of the horizontal scans at different elevation angles to form the scanned volume. For more information about radar applications in meteorology, the reader is referred to Fabry (2015).

Using two radars in synchrony, referred to as dual-Doppler systems, makes retrieval easier compared to using one radar, yet it is harder to achieve as fixed radars are rarely found in vicinity to other radars. Dual-Doppler systems are usually mobile radars used during special field projects to study weather events like thunderstorms (Fujita 1985; Gunter and Schroeder 2015).

Alternatively, estimating wind velocities from one radar requires an assumption to overcome the indeterminacy. The first attempt to do so was proposed by Lhermitte and Atlas (1961). The main assumption of their proposed velocity–azimuth display (VAD) technique is that the analyzed section of the wind field has the same magnitude and direction. Accordingly, fitting the measured radial velocity to a harmonic representation for points along a ring around the radar would allow for computing the wind magnitude and direction. The fitting method is evaluated based on a harmonic wave, where the amplitude and phase shift of the wave correspond to the wind magnitude and direction, respectively. Considering a full azimuthal range yields a single result per scanned level, which can be combined to construct a vertical profile such as the work done by Giammanco et al. (2016) and Krupar et al. (2016). A three-dimensional approach, named volume velocity processing (VVP), was proposed by Waldteufel and Corbin (1979). This approach assumes linear wind within a volume and solves for variables within that volume.

A lot of work has been done based on these two generic techniques of single-Doppler analysis. Researchers like Browning and Wexler (1968) and Siemen and Holt (2000)

built on the VAD technique, while others like Shapiro et al. (2003) and Zhou et al. (2014) proposed retrieval methods based on the VVP technique. Although VAD and VVP are the most widely used approaches for wind retrieval, particularly the works of López Carrillo and Raymond (2011), Li et al. (2017, 2007), Liou et al. (2018), Shapiro et al. (2003), Zhao et al. (2003), and Zhou et al. (2019) provide further insights on the development of wind retrieval methods.

Even though progress on wind retrieval has been made over the years, the challenge of retrieving near-surface peak winds for localized events, like thunderstorms, using fixed radars persists. For example, a comprehensive study that compared retrieved hurricane velocities from fixed radars to ground measurements was presented in the work done by Krupar et al. (2016). However, hurricanes are more abiding to the VAD linearity assumptions when compared to smaller-scale thunderstorm wind events. This limits the generalization of the technique to use with thunderstorms. Furthermore, Liou et al. (2018) used mobile Doppler radars instead of fixed Dopplers to make use of their enhanced temporal and spatial resolution. The study produced realistic retrievals that show fine-scale wind variations in the hook-echo region of a supercell, yet the analyzed data from mobile radars have a limited availability compared to fixed radars, which limits the efforts of developing historical statistics of thunderstorm wind speeds.

One of the most advanced VAD-related techniques was developed by Xu et al. (2006, referred to as Xu06 hereafter). It can retrieve velocities from radar scans through statistical interpolation between neighboring points, allowing for relaxing the assumption of constant velocity throughout the analyzed domain. Nevertheless, the technique relies on relating the measurements from a spatial domain that can be large enough to average out peak wind velocities of thunderstorm events that need a resolution of hundreds of meters to a few kilometers, at most, to be captured. From a statistical perspective, it would be useful to find a technique that utilizes fixed radars, providing extended records (in contrast to mobile radars) and retrieves peak velocities of localized thunderstorm events that are comparable to peak ground measurements.

Therefore, the objective of the current study is to develop a method to retrieve peak wind velocities from scans of fixed

TABLE 1. List of stations used in analysis sorted by distance between radar and ASOS stations.

Radar	ASOS	Radar longitude (°)	Radar latitude (°)	Distance radar to ASOS (km)	Azimuth radar to ASOS (°)	Height difference (m)	Analyzed events of TSRA
KBYX	KNQX	-81.7032	24.5975	2.44	139	45.7	123
KTLH	KTLH	-84.3289	30.3976	2.50	262	57.0	142
KIND	KIND	-86.2804	39.7075	2.71	272	55.1	214
KFSD	KFSD	-96.7294	43.5878	2.84	251	47.1	190
KGRR	KGRR	-85.5449	42.8939	3.00	113	52.8	205
KGRB	KGRB	-88.1111	44.4985	3.26	240	64.8	141
KAMX	KTMB	-80.4127	25.6111	3.59	317	62.6	193
KOKX	KHWV	-72.8639	40.8655	3.76	188	72.8	24
KPBZ	KPIT	-80.2180	40.5317	3.79	206	76.3	65
KCXX	KBTV	-73.1664	44.5110	3.93	152	61.8	82
KSRX	KFSM	-94.3619	35.2904	3.97	351	122.4	143
KLSX	KSUS	-90.6829	38.6987	4.63	140	118.1	214
KLWX	KIAD	-77.4778	38.9754	4.83	136	73.8	126
KILN	KILN	-83.8217	39.4203	5.05	80	72.0	210
KDTX	KPTK	-83.4718	42.7000	6.44	117	127.2	96
KCBW	KHUL	-67.8066	46.0392	7.31	355	172.6	24
KARX	KLSE	-91.1916	43.8228	8.10	307	281.5	189
KAPX	KGLR	-84.7198	44.9071	9.22	11	149.6	97
KLZK	KLIT	-92.2622	34.8365	9.73	162	199.7	238

radars such that they are comparable to peak ground measurements in thunderstorm wind conditions. This will be done by using a piecewise variation of the VAD technique that analyzes a limited spatial domain versus the conventional VAD method that typically analyzes the complete 360° azimuth of Doppler velocities. The resulting data are compared to the advanced VAD technique developed by Xu06, as well as anemometer measurements from the ASOS network to evaluate the usability of radar-retrieved velocities for retrieving peak thunderstorm wind velocities during thunderstorm events.

2. Data structure and utilization

a. Data structure

The National Weather Service’s (NWS) NEXRAD weather radar network is a key tool for storm detection and prediction across the United States. The radar data used are from the NEXRAD level-II archive (NWS 2021b) that combines radar measurements from 160 WSR-88D radars since 1991. Level-II archive provides the finest azimuthal resolution (0.5°), which is influential for the proposed retrieval method. Radar data older than 2012 are single-polarized, after which they gradually changed to dual-polarized until completed in 2014. This change in technology does not affect the homogeneity of the dataset used for this study since no dual-polarization data are used.

Every archived file is annotated by a time stamp corresponding to the start of the scan in UTC. Each file includes horizontal scans taken under (PPI) scanning mode for elevation angles,  $\theta$ , ranging from 0.5° to 19.5°. The radial velocity scans have an azimuthal resolution of 0.5° and a fixed gate spacing of 250 m out to 230 km away from the radar for the lowest elevation angles. For the archived data, the range of elevation angles scanned and their sequence depend on the operating modes—named volume coverage patterns (VCPs)—that are selected by local

weather forecast office based on weather conditions at the time. In cases of severe weather, VCPs that have more repetitions of the lowest angle of elevation are typically used in severe weather operations in order to monitor rapidly changing storm features. The increased frequency of the 0.5° elevation angle scan increases the temporal resolution from 1 per 6 min (the total scan time for each archived volume) to about 1 per 1.5–2 min when repeating the 0.5° scan three or four times per volumetric scan after the addition of Supplemental Adaptive Intravolume Low-Level Scan (SAILS) scans (OFCM 2017).

Anemometer records were taken from National Centers for Environmental Information’s (NCEI) ASOS database. ASOS is a network of over 900 stations covering the United States (NWS 2021a). Each station includes an anemometer at an approximate height of 10 m. ASOS has two data streams: 64010 (5 min), and 64050 (1 min). The resolution represents the archiving frequency while the sampling frequency was at 1 Hz.

b. Data utilization

First, radar and ASOS station combinations were selected such that the ASOS station is between 2.4 and 10 km away from the radar. This minimum distance was used to match the minimum radius of recorded radar data. The elevation angle used in the current study is the lowest available at 0.5°, and the retrieval procedure was limited to 10 km of radial distance. This is because the elevation angle results in an (approximately) 8 m km<sup>-1</sup> slope upward from the radar base. Noting that radars are placed on pedestals with heights of 25 m or more from the ground, the height difference between the scanned radar point and the anemometer would make it hard to correlate retrieved (radar) and measured (anemometer) data beyond 10 km of radial distance. Accordingly, 19 stations were selected, as listed in Table 1. The table also provides the position of each radar station, as plotted in

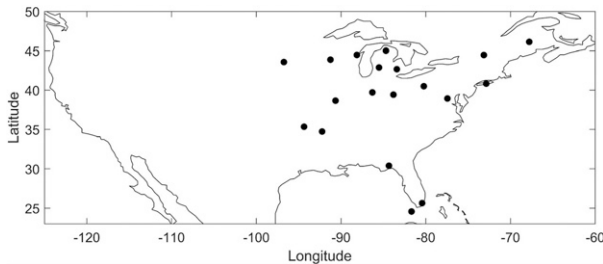


FIG. 2. Locations of radar stations used in the analysis.

Fig. 2, the distance between the radar and ASOS station (in kilometers), the height difference between anemometers and the center point of the radar beam (assuming the beam is a straight line given its close proximity to the radar), and the number of events analyzed for each radar–ASOS combination. Distances between stations were computed based on their longitude–latitude location, while height differences were computed based on ground elevations from Google Earth. It is worth noting that although the stations were only chosen on the basis of availability of ASOS stations that are in close proximity to the radar, the distribution of stations shown in Fig. 2 is similar, to some extent, to the regions where annual maxima of wind speeds are dominated by convective events as per Fig. 3 in Lombardo and Zickar (2019).

The next step was to download ASOS data for the months of April to October for every year between 2000 and 2020. The range of months chosen aligns with the occurrences of extreme events based on analyzing ASOS data as presented by Lombardo and Zickar (2019). The 5-min 64010 data were used to determine the files to download from NEXRAD since one of the recorded fields is an alphanumeric identifier to describe the weather condition. Accordingly, instances of thunderstorm occurrence (TSRA) were identified. Data extending 1 h before the first TSRA and 1 h after the last TSRA were downloaded from the NEXRAD archive for each event. To ensure independence between events, those occurring within 6 h of one another were merged to be one event similar to the procedure implemented in Lombardo and Zickar (2019). Furthermore, the 64050 files included the measured velocities and directions that were used to evaluate the radar-retrieved values. Fields in 64050 files include 3-s and 2-min wind speeds and directions, recorded every minute. Only the 3-s data were used in the current study as the objective is to retrieve peak velocities.

Data used from ASOS archives were not standardized, meaning that they were used as found in the archive. As for radar data, the Py-ART toolkit (Helmus and Collis 2016) was used to process NEXRAD raw data. The toolkit was used to perform dealiasing of the radial velocity readings. The Nyquist velocity, extracted from level-II metadata, is around 20–23  $\text{m s}^{-1}$  for the modes analyzed in the current study (A. Losey-Bailor et al. 2019, meeting presentation). Several dealiasing methods are available in the Py-ART toolkit: 1) unwrap method, 2) region-based method, and 3) four-dimensional Doppler dealiasing (4DD) method. The most comprehensive is the 4DD method, which requires initial conditions (dealiasing readings from a

previous time step or a wind profile) to perform. This would result in cumulative errors, so it was avoided. Alternatively, the unwrap method is relatively fast compared to the region-based method. Nevertheless, a study by Louf et al. (2020) indicates that the unwrap method results in twice the errors produced by the region-based method. Therefore, the region-based method was chosen. To avoid the undesired effects of noise on the corrected velocity, a quantity named velocity texture was computed for the velocity field using a built-in function in the Py-ART toolkit. Based on the values computed, velocity values that corresponded to a texture value of more than 3, where higher values imply higher noise, were removed prior to the dealiasing procedure. The choice of this exclusion limit was based on visual observations of corrected velocity fields. To avoid processing excessive numbers of files, only files that had more than one  $0.5^\circ$  Doppler sweep—VCP 12, 212, 112, 215, 121, and 35—were processed. Yet VCP annotations were only mentioned in data archived after 2013, so this filter was not applied to older data. The dealiasing procedure was performed on the full 230 km range of data but only the velocity field within 200 gate spacings ( $\sim 50$  km) from the radar was exported to netCDF format, which was then read by MATLAB (Mathworks 2021) for further processing.

### 3. Methodology

The methodology to retrieve the velocity magnitude and direction of the dealiasing velocity field is described in this section. Given that the objective is to retrieve peak velocities from a nonuniform wind field, the current method aims to retrieve velocities using the smallest possible spatial domain. Based on the sensitivity analysis presented in section 5, it is proposed that a harmonic fit be performed on  $10^\circ$  segments (20 points of  $0.5^\circ$  resolution) in the azimuthal direction to retrieve wind velocities at points of interest. Being a harmonic fit makes it a variant of the VAD retrieval method with the limited spatial domain being its main characteristic. It is important to acknowledge that wind signatures in radar scans are noisy by nature, which makes it challenging to consider such a limited domain. To minimize the effect of noise on the fitted points, two consequent low-pass filters are applied along the radial direction. The filters were of second order with half power frequency ratios of 0.02 and 0.15 of half the sampling frequency. This corresponds to filtering windows of widths  $7.2^\circ$  and  $54^\circ$ , respectively. These values were chosen such that the larger window establishes continuity for a larger scale and eliminates outliers, and the smaller window establishes further consistency, with less noise, among the points to be fitted. For example, examining Fig. 3, this particular PPI scan shows prevailing background wind as well as a separate event approaching from SSW. The expression “event” is used hereafter to refer to nonbackground wind, or flows that occur on a limited scale compared to background wind occurring at a much larger scale. The measured points along a radial ring are presented in the same figure to show that while the background wind fit reasonably to a harmonic, the section representing the secondary event cannot be represented by the same fit. In addition to the inadequacy of fitting both events

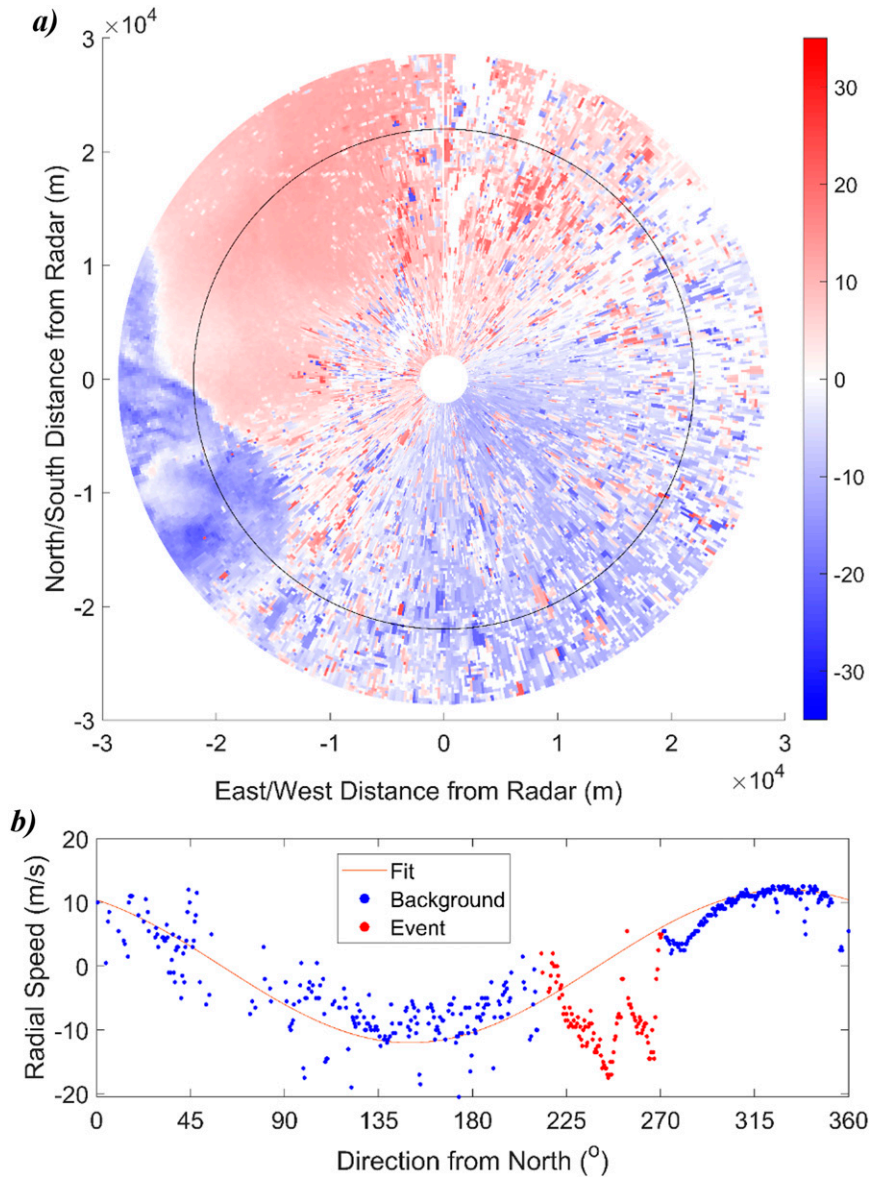


FIG. 3. (a) PPI scan of radial velocity (in  $\text{m s}^{-1}$ ) with a radial ring at  $R_d = 22 \text{ km}$  and (b) measured points along the ring with a harmonic fit. The blue points represent background flow and red points are for event flow.

within the same  $10^\circ$  segment, applying the filtering process along the full radial ring would completely distort the event section, as well as affect the background results. Therefore, it is essential to separate both domains, background and event, prior to the retrieval process.

The separation process relies on the following four steps:

- 1) To remove noise, a grid of  $0.5 \text{ km} \times 0.5 \text{ km}$  is used to remove locations with standard deviation of wind speeds exceeding  $2 \text{ m s}^{-1}$ . Locations with such a high level of inconsistency either represent noise or a sudden change in radial velocity magnitude representing border lines between background and events flows. The removal of

noisy grids is beneficial for the fitting process, while the removal of border regions makes it easier to identify different regions in the next step. Figure 4 shows the PPI scan before and after the removal of inconsistent locations, while Fig. 5 shows the effect of noise removal and filtering on partitioned regions.

- 2) MATLAB's Image Processing Toolbox is used to label different regions for each PPI scan of radial velocity. Considering positive and negative wind speeds separately, the following steps were performed:
  - (i) Image Processing Toolbox functions `imerode` and `imdilate` are applied to the scan. Any data point that is

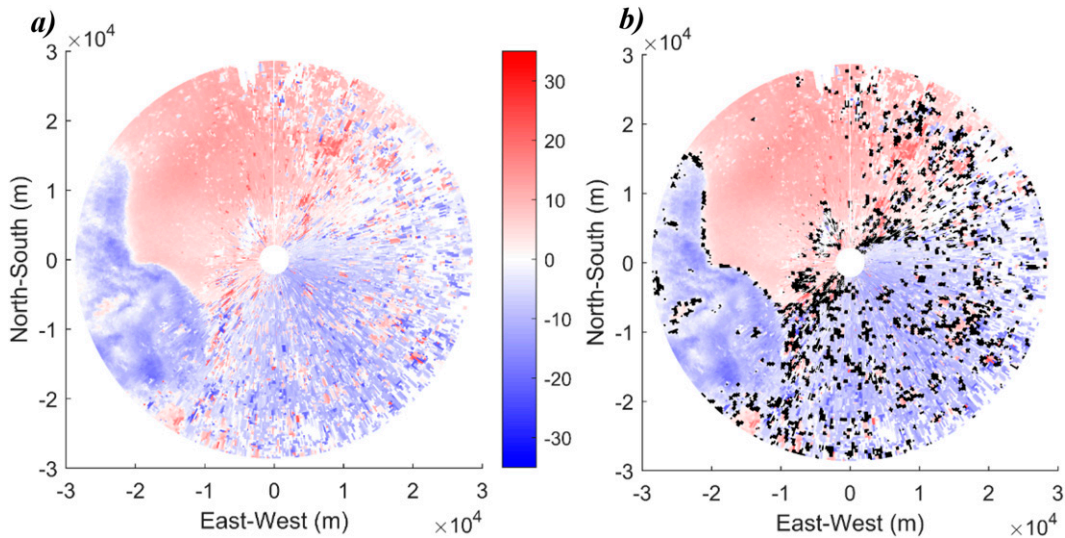


FIG. 4. Effect of noise removal shown using (a) raw scan of radial velocity and (b) noise removed and replaced with black zones.

not neighboring at least another point with valid velocity value was deleted using *imerode*. This procedure is dependent on the removal of inconsistent grid values performed in the previous step which removed data points between different flow regions. Using *imerode* helps widen border lines between regions to facilitate the region labeling in step (ii). After that, *imdilate* is used to connect regions that would fall within a *disk* of five grid points diameter from one another. This helps step (ii) form regions that would otherwise be too small to be valid for the separations on the following steps.

- (ii) Image Processing Toolbox function *regionprops* combines every eight or more connected grid points to form a region. Grid points of each region are then fitted to Eq. (1) which represents a harmonic fit that takes into account the height difference between points introduced by the scanning elevation angle pointing upwards. Assuming the wind vertical profile is exponential, the three fitting parameters would represent the amplitude of the harmonic (wind speed), the phase shift (wind direction), and lastly

the power-law coefficient. Background flows are expected to adhere to the exponential vertical profile, unlike thunderstorm flows. This will be used on a later step to separate thunderstorm flows from background. For further analysis, a few parameters were stored for each region. From the fitting process, the first two fitting parameters, the  $R^2$  value, and the mean absolute residual error were stored. In addition, the area of each region, computed using Eq. (3), was also stored:

$$v_{\text{rad}} = a_1 \times \sin(\phi + a_2) \times \left[ \frac{h(R_d)}{h_{\text{rad}}} \right]^{a_3}, \quad (1)$$

$$h(R_d) = h_{\text{rad}} + R_d \tan(\theta), \quad (2)$$

where  $v_{\text{rad}}$  is the measured radial velocity,  $a_1$  is the first fitting parameter corresponding to amplitude of a harmonic wave,  $\phi$  is the azimuth angle of the data point from the north direction,  $a_2$  is the second fitting parameter corresponding to the harmonic phase shift,  $h(R_d)$  is height of the radar beam

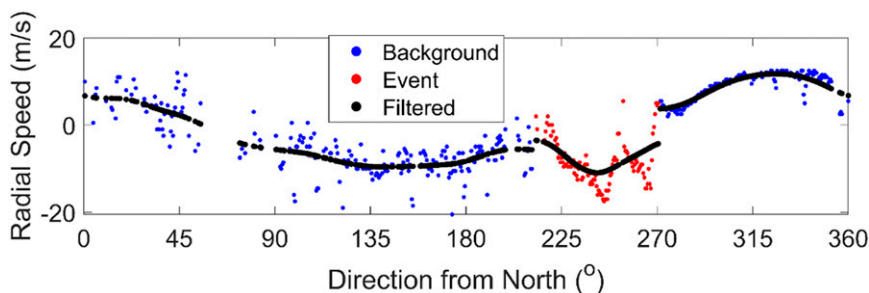


FIG. 5. The effect of noise removal and filtering shown using data points distribution along a ring for the original data, data after noise removal, and data after filtering.

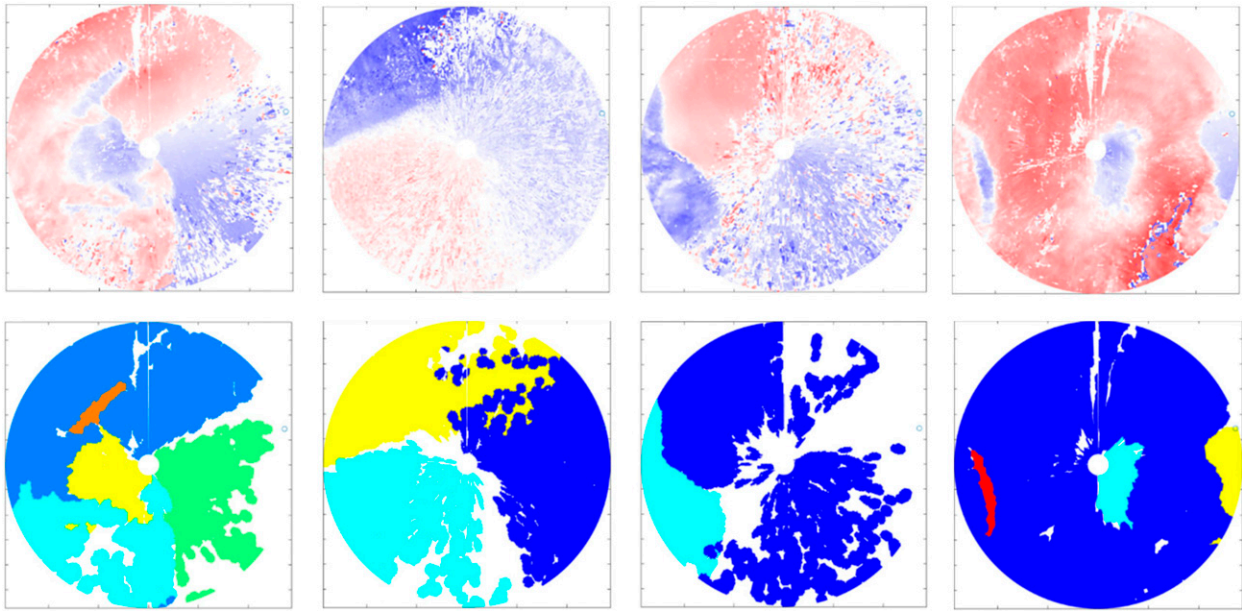


FIG. 6. Examples of classified regions from PPI scans. (top) Radial velocity scans (blue is negative and red is positive) and (bottom) classified regions where each color represents a different region.

above the ground level,  $h_{rad}$  is height of the radar station,  $a_3$  is third fitting parameter representing the power-law coefficient; and  $\theta$  is scanning elevation angle;

$$\text{Area} = \sum_1^{n_{\text{elements}}} \frac{\pi}{n_{\text{az}}} \times \left[ (R_d + \text{gs})^2 - (R_d - \text{gs})^2 \right], \quad (3)$$

where  $n_{\text{elements}}$  is number of elements (grid points) in the region,  $n_{\text{az}}$  is number of points in azimuthal direction (720 for  $0.5^\circ$  resolution),  $R_d$  is radial distance to radar of each element, and “gs” is gate spacing (250 m).

- 3) The main separation of event flow from background flow occurs in this step. An optimization-based technique is used to separate events from background flow as discussed hereafter. Based on the region characteristics computed in the previous step, regions that had (i) area  $> 250 \text{ km}^2$ , (ii)  $R^2 > -1.5$ , and (iii) mean absolute residual error of velocities  $> 2 \text{ m s}^{-1}$  were considered to have events embedded in background flows. The choice of area was such that the area had to be large enough to engulf background wind and an event. Also, it was found that regions with  $R^2 < -1.5$  correspond to regions where no part represents straight background wind in which case the separation algorithm cannot operate (since there is no background region to separate). The same analogy applies for the choice of cutoff error where regions with more than  $2 \text{ m s}^{-1}$  error imply the presence of an area with values that offset from the current fit. An ensemble of more than 100 scans containing event flows within background flows was used to decide on these cutoff values.

Regions with the mentioned features are partitioned using an optimization-based technique. An optimization

function searches for the largest combination of grid points that can be labeled background wind as follows: Optimization parameters:  $a_1$ ,  $a_2$ , and  $a_3$  similar to Eq. (1):

$$\text{Objective function: } \text{Ar} = -\frac{\text{Ar}_{\text{sm-res}}}{2 - R^2}. \quad (4)$$

The optimization is done using MATLAB’s Optimization Toolbox function “patternsearch” with mesh tolerance of 0.01. “Ar” in Eq. (4) is the variable to be minimized, where  $\text{Ar}_{\text{sm-res}}$  represents the area of data points with a smoothed fitting absolute residual not exceeding  $1.5 \text{ m s}^{-1}$ , set to be the characteristic of background wind. Smoothing is performed using the 2D smoothing function “nanmedfilt2” as per Voronov (2021) to avoid the effect of outliers. Last, the area computed is divided by  $(2 - R^2)$  to prioritize areas that have higher conformity. Accordingly, an  $R^2$  value of 1 would result in the lowest (highest negative value) Ar and values would worsen as  $R^2$  decreases. The final  $\text{Ar}_{\text{sm-res}}$  is considered to be the background straight wind subregion and the remaining subregion represents the event flow and is assigned a new region number. Figure 6 shows examples of classified regions in comparison to the radial velocity scans. Examining the velocity scans can lead an experienced meteorologist to identifying the type of event, especially when aided by reflectivity scans. Nevertheless, it is important to note that the presented classification procedure does not aim to do that, but instead aims at separating regions based on their radial velocities to ensure the

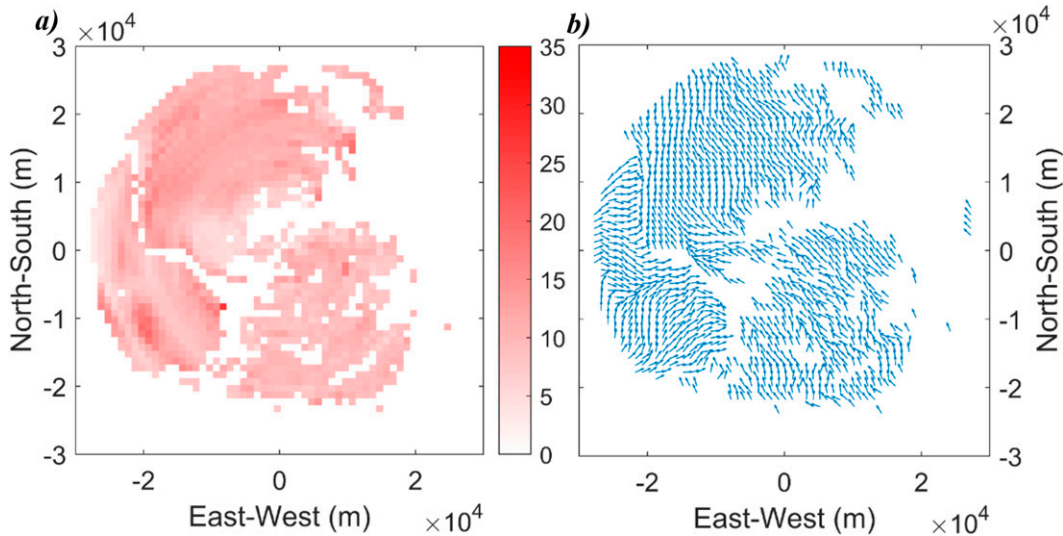


FIG. 7. (a) Magnitude and (b) direction of retrieved velocity using a 1 km grid. White space is an indication of missing raw data or eliminated noise.

harmonic fit is only applied to points that can be assumed to share the same magnitude and direction. For example, the second scan in Fig. 6 shows the background region (in the bottom portion of the scan) divided in two. While they are actually one region, the classification process only ensures that points within each classified region can be assumed to have the same magnitude and direction so VAD assumptions can be applied.

- 4) As a last step in the separation process, the algorithm goes through the classified regions to check for narrow gust fronts. Regions similar to the red region in the last classification of Fig. 6 cannot be fitted on an azimuthal ring with  $10^\circ$  segments as it is exceptionally narrow. Instead, the fit in this case is performed for points within 5 km from the point of interest rather than along an azimuthal ring. This approach yields enough points to evaluate the fit for each point of interest. To classify these regions as narrow gust fronts, the following sub-steps were performed:

- (i) Each region is fitted using least square orthogonal linear fit as per Carr (2021). This is a linear slope and intercept fit that minimizes the local orthogonal residual instead of the global y residual. The resulting root-mean-squared error (rmse) is the thickness of the region. Also, angles  $\psi_1$  and  $\psi_2$  were computed as the slope angle of fitted straight line  $\pm 90^\circ$  to represent the potential directions of wind perpendicular to the fitted line.
- (ii) The length  $l$  of each region along its longer axis is computed using its minimum and maximum global  $x$  and  $y$  coordinates.
- (iii) The processed region is also fitted using Eq. (1) to find  $a_2$ .

- (iv) The region is assigned to be a narrow gust front if it follows the conditions

- 1)  $l > 5000$  m indicating long length,
- 2)  $\text{rmse} < 1200$  m indicating narrow shape,
- 3)  $l/\text{rmse} > 12$  indicating slender shape, and
- 4)  $|a_2 - \psi_1|$  or  $|a_2 - \psi_2| < 20^\circ$  indicating wind direction is perpendicular to longer dimension.

Accordingly, for each PPI scan of radial velocity, the separation algorithm is performed to label regions that would be fitted separately. After that, for any point of interest, the two-step filtering procedure is applied for points that belong to the same region, and last, a  $10^\circ$  segment is fitted to a harmonic fit to find the wind magnitude and direction. Applying these steps to a 1-km resolution grid of points for the scan in Fig. 3, the 2D wind field is presented in Fig. 7 representing (Fig. 7a) the magnitude and (Fig. 7b) the direction of the estimated wind velocities. Different regions can be clearly distinguished based on the predicted directions. This could not be achieved without the separation prior to the harmonic fitting at points of interest. The next section of this study will present more metrics of the retrieved results in comparison to synchronized ASOS results. Retrieval was only performed for one point per scan, aligning with the ASOS station location. Results were also compared to retrievals performed using the advanced VAD technique presented by Xu06 which was processed using the software module developed by Lang et al. (2018).

#### 4. Results and discussion

The procedure elaborated in the methodology section was performed on the radar scans described in the data section. The same radar scans were used for retrieval using the technique proposed by Xu06. Both techniques had similar computational time. Yet it is important to note that the amount of time used by the current technique only yields the fitted

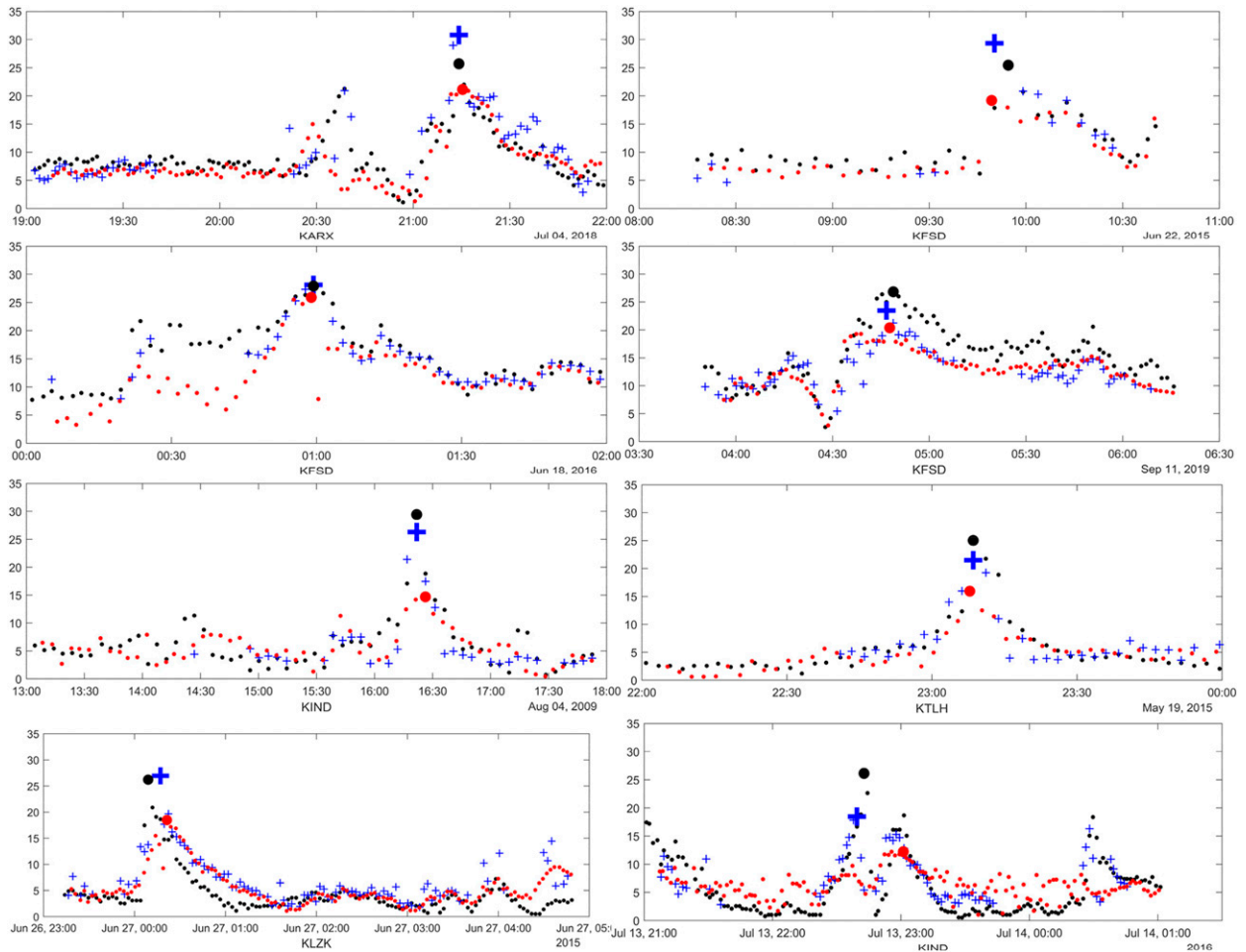


FIG. 8. Time histories of retrieved events showing ASOS record (black dots), XU retrieval (red dots), and current method retrieval (blue crosses). The peak event velocity from each record is shown in larger annotation points.

velocity of a single point, while the same amount of time results in retrieving a grid of points covering the entire domain considered for retrieval within the PPI scan. This means that the new technique is significantly slower than Xu06, which is more suitable for nowcasting applications. The results presented hereafter are statistical comparisons between the retrieved radar velocities using both techniques versus ASOS 3-s measurements.

*a. Comparison between current technique and Xu06*

Figure 8 provides examples for how each of the retrieval techniques perform, depicting eight distinct examples. These chosen time histories all had peak ASOS velocities of at least  $25 \text{ m s}^{-1}$ , which is close to the NWS’s definition of severe winds (58 mph). Several observations can be made. First, it can be seen that the current technique removes some data points that are evident in the ASOS record. All of the missing points occur when the wind speed is of lower magnitude; points with higher magnitudes are always present. This is a by-product of the noise suppression and classification procedures that result

in the removal of data points such that there is a lack of sufficient data to perform the fit within the  $10^\circ$  segment width. Since higher magnitude wind speeds are unaffected, which aligns with the objective of this study, this loss of data at low speeds is not deemed to be important.

Second, when examining the peak speeds from each record, it is observed that the current technique is always closer to the ASOS peak value than Xu06. This is expected due to the spatial domain adopted by each technique. The current technique relies on a limited domain of  $10^\circ$  width, equivalent to hundreds of meters in scale, while the other technique adopts a domain that is two orders of magnitude larger. Although the Xu06 method results in almost no missing point in the records, it inherently performs spatial averaging that smooth out peak velocities due to the larger size of the considered spatial domain. To confirm this, we altered the correlation length with the Xu06 technique, going as low as 5 km instead of the 60 km used in their study, which did not alter the results significantly. Thus, the Xu06 methodology is not appropriate for determining peak event wind speeds.

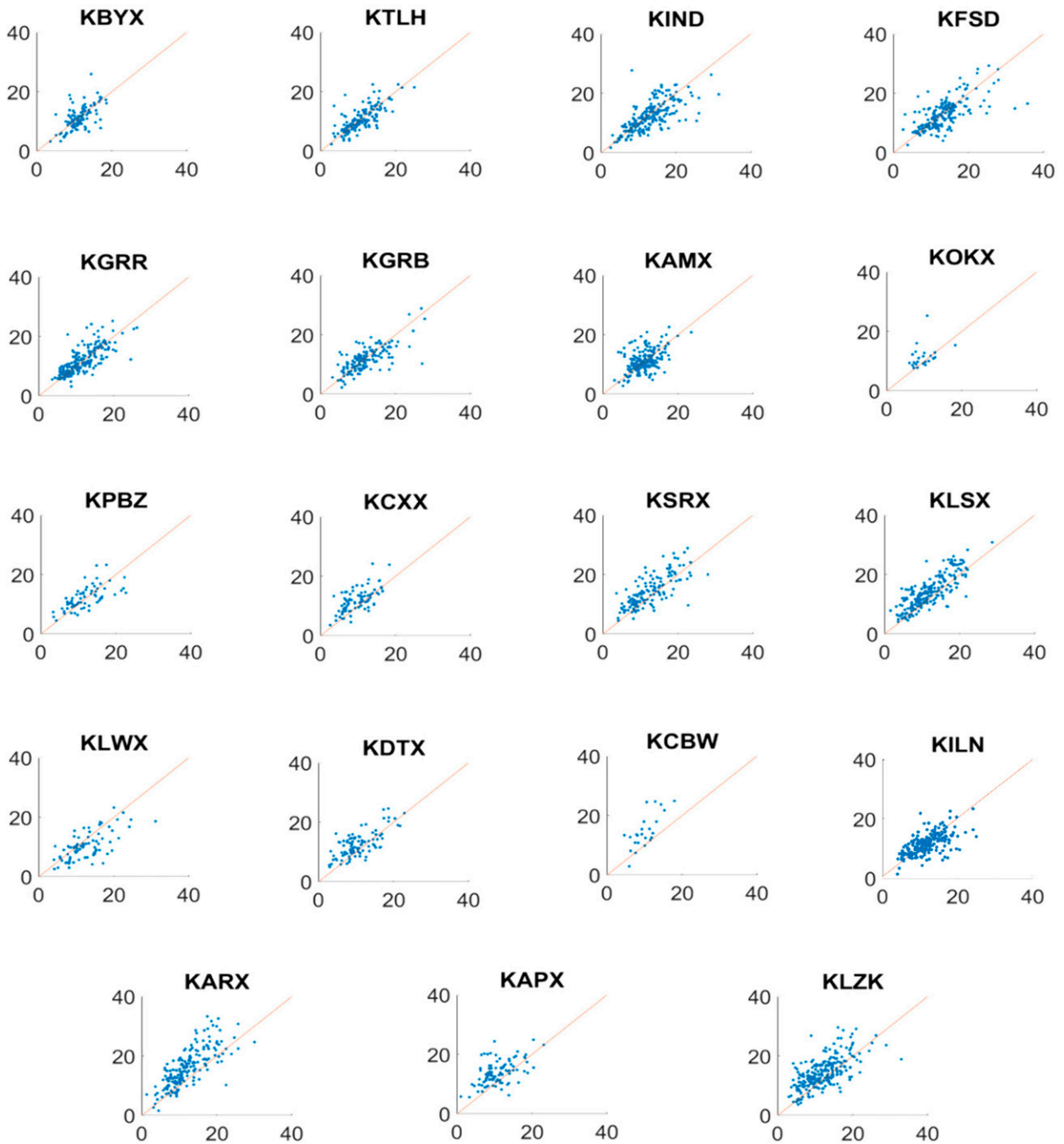


FIG. 9. Peak event retrieved velocity (y axis) vs ASOS (x axis) for each station separately (in  $\text{m s}^{-1}$ ).

#### b. Assessment of retrieved peak velocities

In this section, peak event velocities obtained from the current technique are examined to assess the validity of relying on radar retrievals for estimating peak thunderstorm event velocities. ASOS ground measurements are used for comparison. Figure 9 shows the peak event velocities estimated for each station using the current method and from the ASOS stations. Each diagram also has a 1:1 line to judge the relevance of the retrieved

velocities. The stations are sorted by their distance separation from the radar. The axes represent ASOS and radar for  $X$  and  $Y$ , respectively. The remainder of this section will explore the properties of the computed peak velocities with relation to distance and height difference.

To compare the radar and ASOS data, it is important to acknowledge two features of radar retrievals: (i) the scanned volumes are at a higher elevation than the anemometer masts,

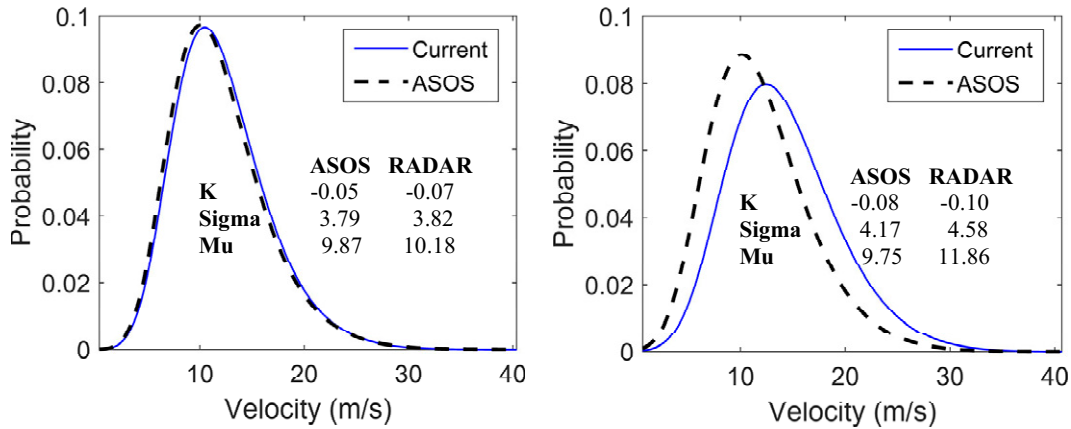


FIG. 10. Peak event velocity distribution fits for stations (left) within 4 km and (right) more than 4 km.

which are at 10 m, and (ii) the scanned volumes vary with distance from the radar. The elevation of the scanned volume is generally proportional to the distance from the radar as a result of the scanning elevation angle. It is also affected by the ground elevation at the radar base compared to the ground elevation for the scanned volume, as demonstrated in the values of Table 1, which do not follow a monotonic trend with distance. It is expected that higher elevation would lead to overestimation of retrieved velocities compared to ASOS due to the boundary layer frictional effects. In contrast, due to the beamwidth increasing as the distance from the radar increases, the resolved volume increases as a function of distance, which is expected to underestimate the retrieved velocities as it represents a volume in the case of radar versus a point in the case of anemometers. As per Eq. (5), assuming a pulse duration of 2  $\mu$ s, which is in line with the 1.5–2.5  $\mu$ s operational range of NEXRAD radars, a 1°-wide beam would result in a resolution volume that varies between 0.36 and 9.1 km<sup>3</sup> for radial distances of 2 and 10 km, respectively (Wolff 2022). These volumes are significant particularly when compared to ASOS resolution volume, which is essentially a point:

$$\text{Volume} = R_d^2 \theta_b^2 \frac{c\tau}{2}, \tag{5}$$

where  $R_d$  is radial distance from radar,  $\theta_b$  is beamwidth in radians,  $C$  is the speed of light, and  $\tau$  is pulse duration.

To observe the effects of the distance from the radar on the estimated peak velocities with the current method, Fig. 10 shows the generalized extreme value distribution fit for stations less than 4 km away from the radar (left panel) and stations more than 4 km away (right panel). The closer stations had a much better agreement compared to stations farther away. Nevertheless, it is important to note that the retrieved peaks had a distribution that is to the right of the ASOS distribution. This means that the current retrieval technique overestimates the peak velocities as distance increases, leading to the conclusion that height increase effect overrides the volume averaging effect. While height is related to distance away from the radar, the initial height difference (radar height – ASOS height) results in a different relation for each station combination. Therefore, height and distance are examined independently. A more detailed look into the height effect can help refine the retrieved velocities.

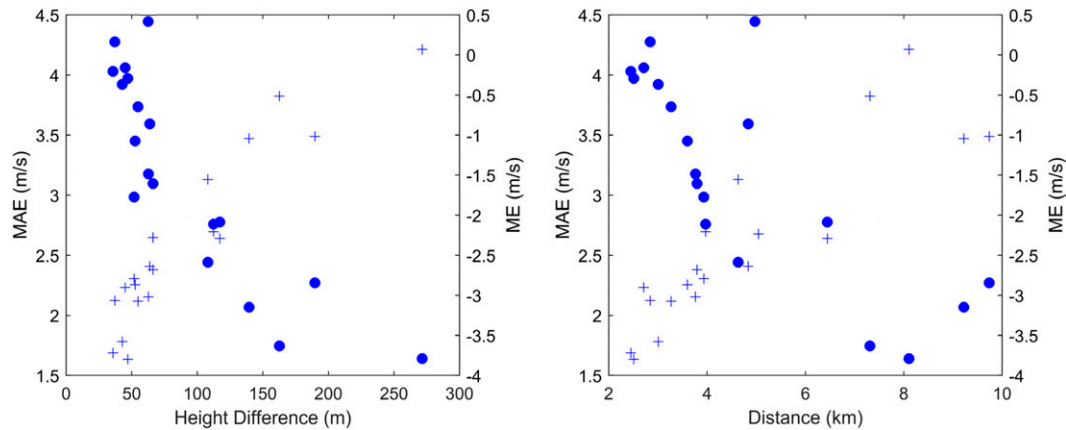


FIG. 11. Velocity mean errors (dots) and mean absolute errors (crosses) vs (a) height difference between the beam and ASOS anemometer and (b) distance between the ASOS and radar.

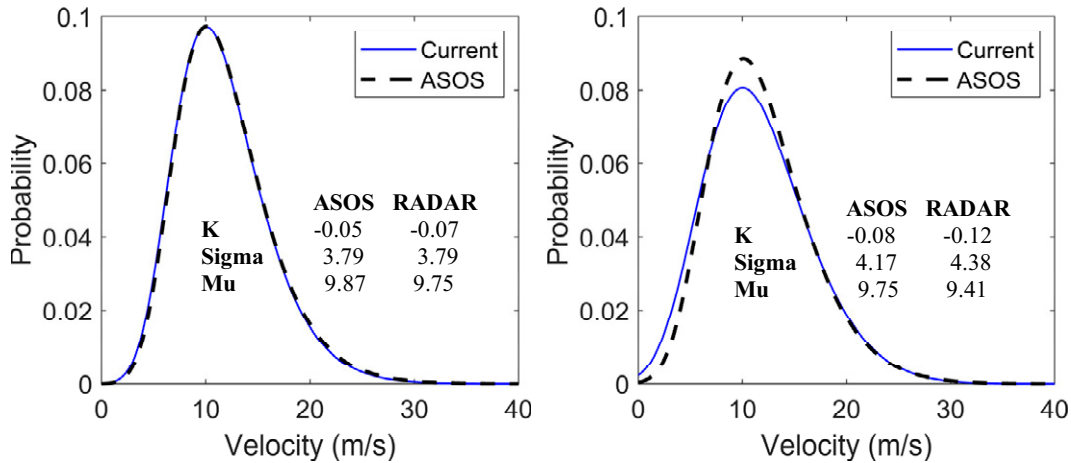


FIG. 12. Peak event velocity distribution fits for stations (left) within 4 km and (right) more than 4 km after correction using error in Eq. (6).

Accordingly, Fig. 11 examines the mean error and mean absolute error of velocity, being the difference between ASOS and retrieved values, plotted against height difference (left panel) and distance (right panel). These error values were computed from all retrieved points rather than only peak points used for previous comparisons. The figure shows, as expected, an increase in mean absolute errors with height and distance ranging between 1.6 and 4.2  $\text{m s}^{-1}$ , as well as a decrease for mean errors going from 0.5 to  $-4 \text{ m s}^{-1}$ .

A closer look at the plotted values shows that the mean error plotted against height difference would comply to an exponential fit. Given that the previous discussion showed that distance is less important to errors compared to height, it was decided to use the distribution of error with height to correct the retrieved peak velocities. The trend in the case of mean error versus height difference is close to an exponential representation. Fitting the mean error versus height  $h$  using Eq. (6) result in fitting parameters equal to  $-0.173$ ,  $37.38$ , and  $1.71$  for parameters  $a$ ,  $b$ , and  $c$ , respectively:

$$\text{Err} = a \times \left( \frac{h - b}{10} \right)^{1/c}. \quad (6)$$

Modifying the retrieved peak event velocities plotted in Fig. 10 resulted in the distributions plotted in Fig. 12 based on this error distribution. The modified distribution shows a near-perfect match for stations less than 4 km apart, and a much better agreement for farther stations, especially for the leading tail which is in perfect agreement for values exceeding  $15 \text{ m s}^{-1}$ . The improved range is of more importance given that the objective of this study is to retrieve peak velocities, meaning that higher values are of more relevance.

## 5. Sensitivity and limitations

The proposed algorithm inherently removes data points during noise removal as well as when performing the first step in region classification. The black spaces in Fig. 5 show that

data points that have radial velocity values were eliminated by noise removal procedures. The ASOS data used for comparisons made in the previous section were only ASOS readings that had corresponding radar retrievals. Accordingly, means that ASOS data points that synchronized with missing radar data were removed from the compared dataset. For atmospheric science and wind engineering applications, it is crucial to guarantee that such eliminations did not include any high-intensity peak velocities. To check that, Fig. 13 compares the full dataset of ASOS readings with no eliminations with the dataset used in the previous section for stations with radial distance within 4 km. As illustrated in the figure, the postpeak region is in perfect match, while the main difference is in velocities less than around  $7 \text{ m s}^{-1}$ . It is reassuring that results of radar retrieval do not miss important data of higher intensity and can predict it within the errors described above.

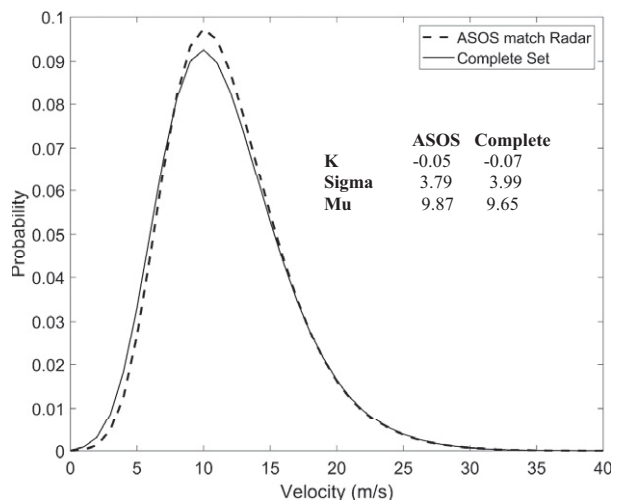


FIG. 13. Peak event velocity distribution fits for complete ASOS set and radar matching set where data points corresponding to missing radar data were eliminated.

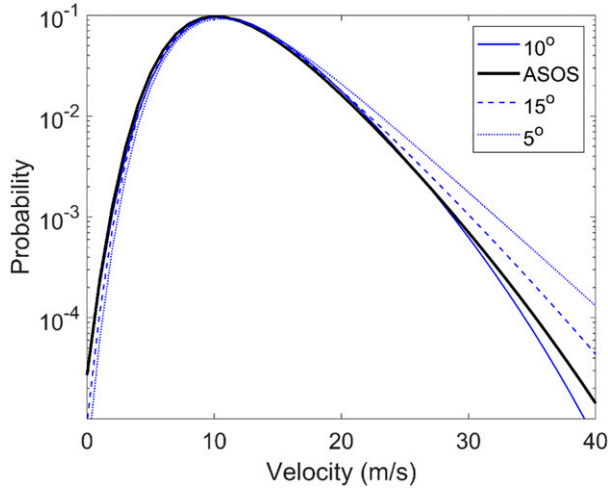


FIG. 14. Peak event velocity distribution fits using different fitting segment widths.

Furthermore, fitting the data points to a harmonic wave was done using a segment width of  $10^\circ$ . This choice was based on comparing the distribution functions of retrieved data with ASOS data for radial distances of 4 km or less as shown in Fig. 14. Visual comparison shows that the  $10^\circ$  segment width results in more conforming results with ASOS observations compared to  $5^\circ$  and  $15^\circ$  segment widths. The y axis is presented on a log scale to amplify the differences for comparison.

In addition, the chosen segment width of  $10^\circ$  influences the minimum scale resolvable by the retrieving technique. The  $10^\circ$  segment is assumed to have wind flow with the same magnitude and direction. Yet diffluent flow, which is a common feature of thunderstorm outflows, will see error introduction as the linearity assumption is violated. To investigate the scale of error introduced in such nonlinear flows, retrieval using  $10^\circ$  segments was performed on a static representation of the analytical model presented by Xhelaj et al. (2020). The model represents directionally diverging flow due to stagnation of a vertical downdraft. As explained in their work, the wind field is a function of the maximum velocity  $v_{\max}$ , the radial position away from the stagnation center  $r$ , as well as event descriptors  $R_{\max}$  and  $R_s$ . The two event descriptors represent the radius of maximum velocity and the radial length scale, both of which are functions of the downdraft radius  $R_{\text{down}}$ . Equation (7) explains how the radial velocity  $v(r)$  is computed:

$$v(r) = \begin{cases} v_{\max} \left( \frac{r}{R_{\max}} \right), & 0 \leq r \leq R_{\max} \\ v_{\max} \cdot \exp \left[ - \left( \frac{r - R_{\max}}{R_s} \right)^2 \right], & R_{\max} < r \end{cases}, \quad (7)$$

where  $R_{\max} = 2R_{\text{down}}$  and  $R_s = R_{\text{down}}$ .

The model was used to generate downdraft wind fields with  $R_{\text{down}} = [0.1, 0.25, 0.5, 1, 2, 5, 10]$  km. Each downdraft wind field was applied at a radial distance from the radar varying from 2 to 20 km with 2 km interval. The results shown in

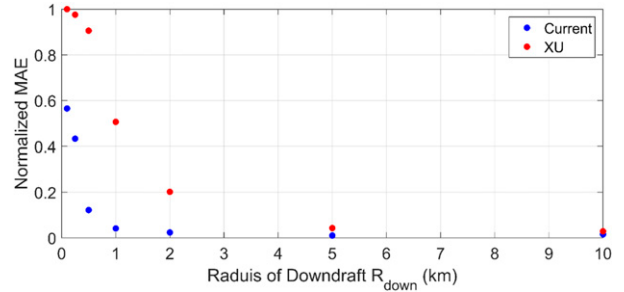


FIG. 15. Normalized mean absolute error of retrieved velocity using  $10^\circ$  segment vs radial distance from the radar.

Fig. 15 show the mean absolute error of retrieved velocity at points of maximum intensity (across varying radial distances) normalized by  $v_{\max}$  versus the downdraft radius in kilometers. It can be noted that the error decays exponentially with the increase of downdraft radius for both cases. The current technique outperforms the other one, especially for smaller radii due to the smaller spatial domain considered in the analysis. It is also important to note that the simulated downdraft did not include any noise, which means that the errors computed are for the peak performance of the retrieval algorithm. The introduction of noise would increase the error. The current technique is shown to yield less than 5% normalized error at 1 km radius, which the other technique achieves at 5 km radius. Nevertheless, due to the noise removal and classification associated with the current algorithm, it is suggested that it cannot be reliable for flows that diverge with radii less than 3 km, which corresponds to region area of  $25 \text{ km}^2$ .

Furthermore, it is important to note that the presented results are bound by the specific properties of WSR-88D radars and the archiving features of level-II data. Different radar products can use the methodology as a concept, but thresholds and limitations need to be changed based on the available data. Last, the presented work does not address factors like terrain roughness and atmospheric stability due to the absence of a clear model that considers both factors when computing vertical wind velocity profiles for thunderstorms. With the presence of such model, these factors can be included in the presented framework in the future.

## 6. Conclusions

The current study presents a method by which a variant of the VAD retrieval method may be applied to thunderstorm winds, which are sampled by high-resolution NEXRAD radar scans, to retrieve peak event velocities. This novel approach overcomes the violation of VAD's linearity requirement in the case of thunderstorm winds by (i) considering a relatively limited spatial domain ( $10^\circ$  segment in the azimuthal direction) and (ii) utilizing image processing and optimization to separate inconsistent flows within each PPI scan such that each flow region can be treated separately. An optimization process identifies the largest area within the region of interest that satisfies specified fitting conditions to a harmonic fit. This

identified area, considered to be background wind, is partitioned from the remainder of the region, considered to be thunderstorm event winds.

To validate the retrieval procedure, estimated velocities were compared to an advanced VAD variant proposed by Xu06, as well as synchronized ASOS 3-s gust measurements at times when ASOS logs indicate the presence of a thunderstorm. A total of 19 NEXRAD–ASOS station combinations having a separation distance of 2–10 km were considered. Between the years 2000 and 2020, more than 2600 thunderstorm events were logged by these 19 ASOS stations. For each thunderstorm event, an average of 45 low-elevation PPI scans were retrieved, resulting in a total of about 117 000 retrieved scans.

The following conclusions can be drawn:

- 1) Retrievals from the presented technique, although computationally expensive, had better estimates of peak velocities compared to retrievals using the method of Xu06. This is attributed to the large spatial domain adopted by Xu06 resulting in underestimation of peak event velocities, especially for higher wind speeds.
- 2) Differences between the retrieved NEXRAD velocities and ASOS 3-s gust measurements showed a clear correlation with both the separation between radar and ASOS station and the elevation difference between ASOS mast and corresponding radar target. The mean absolute error in wind velocity varied linearly between 1.6 and 4.2 m s<sup>-1</sup> for heights and distances in the range of 45–280 m and 2–10 km, respectively.
- 3) Peak event velocity distributions indicate close agreement for stations less than 4 km from the radar. A correction based on the mean error with height significantly improved the peak distributions for all stations, especially for the tails, which are significant for estimating high-intensity wind velocities based on historical records.
- 4) Sensitivity analyses, which are specifically related to WSR-88D data, showed that a 10° radial segment demonstrated the best agreement with ASOS measurements, and that the algorithm can retrieve velocities for diffluent flows with radii as small as 3 km, corresponding to areas of at least 25 km<sup>2</sup>.

These findings suggest that the algorithm can be used to estimate surface wind velocities within 10 km of a radar station. This allows the possibility of retrieving velocities on a spatial grid, which can aid atmospheric scientists studying mesoscale events since the algorithm can reveal details of near-surface flows. Such grid retrievals are also useful for wind engineers in the design of structures with large spatial footprints, such as transmission lines, long span bridges, and large industrial complexes.

*Acknowledgments.* The authors would like to acknowledge the access to computational resources and technical support provided by Compute Canada. The first author is grateful to Natural Science and Engineering Research Council of Canada (NSERC) for financial support through the Vanier Canada Graduate Scholarship. The authors gratefully acknowledge the

financial support provided by ImpactWX and Western University to the Northern Tornadoes Project.

*Data availability statement.* Datasets analyzed in the current study are available in the ASOS (<https://www.weather.gov/asos/>) and NEXRAD (<https://www.weather.gov/nl2/NEXRADView>) web pages. These datasets were derived from the following public domain resources: [/pub/data/asos-fivemin/](https://pub/data/asos-fivemin/), [/pub/data/asos-onemin/](https://pub/data/asos-onemin/), and <https://s3.amazonaws.com/noaa-nexrad-level2/index.html>.

## REFERENCES

- Browning, K. A., and R. Wexler, 1968: The determination of kinematic properties of a wind field using Doppler radar. *J. Appl. Meteor.*, **7**, 105–113, [https://doi.org/10.1175/1520-0450\(1968\)007<0105:TDOKPO>2.0.CO;2](https://doi.org/10.1175/1520-0450(1968)007<0105:TDOKPO>2.0.CO;2).
- Carr, F., 2021: Orthogonal linear regression. MATLAB Central File Exchange, <https://www.mathworks.com/matlabcentral/fileexchange/16800-orthogonal-linear-regression>.
- Duranona, V., 2015: The significance of non-synoptic winds in extreme wind climate of Uruguay. *14th Int. Conf. on Wind Engineering*, Porto Alegre, Brazil, ICWE.
- FAA, 2021: Surface weather observation stations: ASOS/AWOS. FAA, [https://www.faa.gov/air\\_traffic/weather/asos/](https://www.faa.gov/air_traffic/weather/asos/).
- Fabry, F., 2015: *Radar Meteorology*. 1st ed. Cambridge University Press, 272 pp.
- Fujita, T. T., 1985: The downburst: Microburst and macroburst. University of Chicago Projects NIMROD and JAWS Rep., 122 pp.
- Giammanco, I. M., J. L. Schroeder, F. J. Masters, P. J. Vickery, R. J. Krupar, and J.-A. Balderrama, 2016: Influences on observed near-surface gust factors in landfalling U.S. Gulf Coast hurricanes: 2004–08. *J. Appl. Meteor. Climatol.*, **55**, 2587–2611, <https://doi.org/10.1175/JAMC-D-16-0053.1>.
- Gomes, L., and B. J. Vickery, 1976: On thunderstorm wind gusts in Australia. *Civ. Eng. Trans. Inst. Eng.*, **18**, 33–39.
- Gunter, W. S., and J. L. Schroeder, 2015: High-resolution full-scale measurements of thunderstorm outflow winds. *J. Wind Eng. Ind. Aerodyn.*, **138**, 13–26, <https://doi.org/10.1016/j.jweia.2014.12.005>.
- Helmus, J. J., and S. M. Collis, 2016: The Python ARM Radar Toolkit (Py-ART), a library for working with weather radar data in the Python programming language. *J. Open Res. Software*, **4**, e25, <https://doi.org/10.5334/jors.119>.
- Krupar, R. J., J. L. Schroeder, D. A. Smith, S.-L. Kang, and S. Lorsolo, 2016: A comparison of ASOS near-surface winds and WSR-88D-derived wind speed profiles measured in land-falling tropical cyclones. *Wea. Forecasting*, **31**, 1343–1361, <https://doi.org/10.1175/WAF-D-15-0162.1>.
- Lang, T., J. Oguya, J. Hardin, and R. Gupta, 2018: SingleDop 2D retrieval software module. GitHub, <https://github.com/nasa/SingleDop>.
- Lhermitte, R. M., and D. Atlas, 1961: Precipitation motion by pulse Doppler radar. Preprints, *Ninth Conf. on Radar Meteorology*, Kansas City, MO, Amer. Meteor. Soc., 218–223.
- Li, N., M. Wei, X. Tang, and P. Pan, 2007: An improved velocity volume processing method. *Adv. Atmos. Sci.*, **24**, 893–906, <https://doi.org/10.1007/s00376-007-0893-0>.
- , —, Y. Yu, and W. Zhang, 2017: Evaluation of a support vector machine-based single-Doppler wind retrieval algorithm. *J. Atmos. Oceanic Technol.*, **34**, 1749–1761, <https://doi.org/10.1175/JTECH-D-16-0199.1>.

- Liou, Y.-C., H. B. Bluestein, M. M. French, and Z. B. Wienhoff, 2018: Single-Doppler velocity retrieval of the wind field in a tornadic supercell using mobile, phased-array, Doppler radar data. *J. Atmos. Oceanic Technol.*, **35**, 1649–1663, <https://doi.org/10.1175/JTECH-D-18-0004.1>.
- Lombardo, F. T., and A. S. Zickar, 2019: Characteristics of measured extreme thunderstorm near-surface wind gusts in the United States. *J. Wind Eng. Ind. Aerodyn.*, **193**, 103961, <https://doi.org/10.1016/j.jweia.2019.103961>.
- , J. A. Main, and E. Simiu, 2009: Automated extraction and classification of thunderstorm and non-thunderstorm wind data for extreme-value analysis. *J. Wind Eng. Ind. Aerodyn.*, **97**, 120–131, <https://doi.org/10.1016/j.jweia.2009.03.001>.
- López Carrillo, C., and D. J. Raymond, 2011: Retrieval of three-dimensional wind fields from Doppler radar data using an efficient two-step approach. *Atmos. Meas. Tech.*, **4**, 2717–2733, <https://doi.org/10.5194/amt-4-2717-2011>.
- Louf, V., A. Protat, R. C. Jackson, S. M. Collis, and J. J. Helmus, 2020: UNRAVEL: A robust modular velocity dealiasing technique for Doppler radar. *J. Atmos. Oceanic Technol.*, **37**, 741–758, <https://doi.org/10.1175/JTECH-D-19-0020.1>.
- Mason, M. S., 2015: A probabilistic method for estimating regional windstorm occurrence frequency. *14th Int. Conf. on Wind Engineering*, Porto Alegre, Brazil, ICWE.
- Masters, F. J., P. J. Vickery, P. Bacon, and E. N. Rappaport, 2010: Toward objective, standardized intensity estimates from surface wind speed observations. *Bull. Amer. Meteor. Soc.*, **91**, 1665–1682, <https://doi.org/10.1175/2010BAMS2942.1>.
- Mathworks, 2021: MATLAB. Mathworks, <https://www.mathworks.com/products/matlab.html>.
- NWS, 2021a: Automated Surface Observing Systems. NWS, <https://www.weather.gov/asos/>.
- , 2021b: Next Generation Weather Radar (NEXRAD). NOAA, <https://www.ncei.noaa.gov/products/radar/next-generation-weather-radar>.
- OFCM, 2017: Operational modes and volume coverage patterns. WSR-88D meteorological observations: Part C: WSR-88D products and algorithms, Federal Meteorological Handbook FCM-H11C-2017, 5-1–5-24, <https://www.icams-portal.gov/resources/ofcm/fmh/FMH11/fmh11partC.pdf>.
- Riera, J. D., and L. F. Nanni, 1989: Pilot study of extreme wind velocities in a mixed climate considering wind orientation. *J. Wind Eng. Ind. Aerodyn.*, **32**, 11–20, [https://doi.org/10.1016/0167-6105\(89\)90012-3](https://doi.org/10.1016/0167-6105(89)90012-3).
- Shapiro, A., P. Robinson, J. Wurman, and J. Gao, 2003: Single-Doppler velocity retrieval with rapid-scan radar data. *J. Atmos. Oceanic Technol.*, **20**, 1758–1775, [https://doi.org/10.1175/1520-0426\(2003\)020<1758:SVRWRR>2.0.CO;2](https://doi.org/10.1175/1520-0426(2003)020<1758:SVRWRR>2.0.CO;2).
- Siemen, S., and A. R. Holt, 2000: A modified VAD technique for analysing wind fields with Doppler radar. *Phys. Chem. Earth*, **25B**, 1201–1204, [https://doi.org/10.1016/S1464-1909\(00\)00178-7](https://doi.org/10.1016/S1464-1909(00)00178-7).
- Thom, H. C. S., 1968: Toward a universal climatological extreme wind distribution. *Second Int. Conf. on Wind Effects on Buildings and Structures*, Ottawa, ON, Canada, National Research Council of Canada, 669–683.
- Vallis, M. B., A. M. Loredou-Souza, V. Ferreira, and E. de Lima Nascimento, 2019: Classification and identification of synoptic and non-synoptic extreme wind events from surface observations in South America. *J. Wind Eng. Ind. Aerodyn.*, **193**, 103963, <https://doi.org/10.1016/j.jweia.2019.103963>.
- Voronov, R., 2021: nanmedfilt2. MATLAB Central File Exchange, <https://www.mathworks.com/matlabcentral/fileexchange/41457-nanmedfilt2>.
- Waldteufel, F., and H. Corbin, 1979: On the analysis of single-Doppler radar data. *J. Appl. Meteor.*, **18**, 532–542, [https://doi.org/10.1175/1520-0450\(1979\)018<0532:OTAOSD>2.0.CO;2](https://doi.org/10.1175/1520-0450(1979)018<0532:OTAOSD>2.0.CO;2).
- Wolff, C., 2022: Pulse resolution volume. Radartutorial.edu, [https://www.radartutorial.eu/01.basics/The\\_resolution\\_cell.en.html](https://www.radartutorial.eu/01.basics/The_resolution_cell.en.html).
- Xhelaj, A., M. Burlando, and G. Solari, 2020: A general-purpose analytical model for reconstructing the thunderstorm outflows of travelling downbursts immersed in ABL flows. *J. Wind Eng. Ind. Aerodyn.*, **207**, 104373, <https://doi.org/10.1016/j.jweia.2020.104373>.
- Xu, Q., S. Liu, and M. Xue, 2006: Background error covariance functions for vector wind analyses using Doppler-radar radial-velocity observations. *Quart. J. Roy. Meteor. Soc.*, **132**, 2887–2904, <https://doi.org/10.1256/qj.05.202>.
- Zhang, S., G. Solari, Q. Yang, and M. P. Repetto, 2018: Extreme wind speed distribution in a mixed wind climate. *J. Wind Eng. Ind. Aerodyn.*, **176**, 239–253, <https://doi.org/10.1016/j.jweia.2018.03.019>.
- Zhao, K., G. Liu, W. Ge, R. Dang, and T. Takeda, 2003: Retrieval of single-Doppler radar wind field by nonlinear approximation. *Adv. Atmos. Sci.*, **20**, 195–204, <https://doi.org/10.1007/s00376-003-0004-9>.
- Zhou, S., W. Ming, W. Lijun, Z. Chang, and Z. Mingxu, 2014: Sensitivity analysis of the VVP wind retrieval method for single-Doppler weather radars. *J. Atmos. Oceanic Technol.*, **31**, 1289–1300, <https://doi.org/10.1175/JTECH-D-13-00190.1>.
- Zhou, X., L. He, Z. He, and Z. Tang, 2019: Multiresolution and velocity vector average processing algorithm for wind field retrieval based on Doppler radar. *J. Appl. Remote Sens.*, **13**, 046514, <https://doi.org/10.1117/1.JRS.13.046514>.